ACCSCIENCE PUBLISHING

Microbes & Immunity

ORIGINAL RESEARCH ARTICLE

# *In silico* docking and pharmacokinetic evaluation of African ethnomedicinal phytochemicals as dual-target inhibitors of multidrug-resistant Gram-negative bacteria

**Kanayo Samuel Okonji[1]* and Prachi Dash[2]**

[1]Department of Chemistry, Faculty of Science, Federal University Otuoke, Yenagoa, Bayelsa State, Nigeria

[2]Department of Biotechnology, Faculty of Science and Humanities, SRM Institute of Science and Technology, Chennai, Tamil Nadu, India

(This article belongs to the *Special Issue: Natural Products in the Prevention and Treatment of Microbiological, Immunological, and Infectious Diseases: Integrating Wild Edible Plants and Beyond*)

## Abstract

The emergence of multidrug-resistant (MDR) Gram-negative bacteria, including *Escherichia coli* and *Pseudomonas aeruginosa*, poses a critical global health challenge, necessitating innovative antimicrobial strategies. Leveraging Africa's rich phytochemical diversity, this study integrates molecular docking and *in silico* pharmacokinetic profiling to identify natural compounds with dual-target potential. Ten bioactive phytochemicals from ethnomedicinal plants were screened against four validated bacterial targets: LasR (2UV0), AcrB efflux pump (5NC5), DNA gyrase B (6F86), and TEM-1 β-lactamase (1BTL) with AutoDock Vina implemented in PyRx, and the resulting protein–ligand interactions analyzed in Discovery Studio. Docking identified luteolin as exhibiting the highest binding affinity for LasR (−10.8 kcal/mol) and TEM-1, indicating dual inhibition of quorum sensing and β-lactamase activity. Rutin (−9.2 kcal/mol) exhibited high affinity for AcrB, indicating potential efflux pump inhibition, while ellagic acid (−8.3 kcal/mol) targeted DNA gyrase, potentially impairing bacterial replication. Absorption, distribution, metabolism, excretion, and toxicity analyses, along with ProTox-3 predictions, indicated that luteolin exhibited high gastrointestinal absorption and moderate systemic toxicity. Ellagic acid exhibited excellent biocompatibility, whereas rutin showed favorable drug-likeness but low permeability. Collectively, luteolin, rutin, and ellagic acid emerged as promising computational leads with complementary inhibitory mechanisms. This study highlights the translational potential of African phytochemical scaffolds in rational, computer-aided antimicrobial design and provides a foundation for subsequent *in vitro* and *in vivo* validation toward novel anti–MDR therapeutics.

***Keywords:*** Luteolin; Rutin; Ellagic acid; Multidrug resistance; Gram-negative bacteria; Molecular docking; ADMET; African medicinal plants

***Corresponding author:**
Kanayo Samuel Okonji
(kanayosamuelokonji63@gmail.com)

**Citation:** Okonji KS, Dash P. In silico docking and pharmacokinetic evaluation of African ethnomedicinal phytochemicals as dual-target inhibitors of multidrug-resistant Gram-negative bacteria. *Microbes & Immunity*. 2026;3(1):112-132. doi: 10.36922/MI025370100

**Received:** September 9, 2025

**Revised:** October 28, 2025

**Accepted:** November 4, 2025

**Published online:** November 24, 2025

## 1. Introduction

The global emergence of antimicrobial-resistant microorganisms poses a severe threat to public health and food security, largely due to the proliferation of multidrug-resistant (MDR) Gram-negative bacteria such as *Escherichia coli*, *Klebsiella pneumoniae*, and *Pseudomonas aeruginosa*.[1] These pathogens have evolved through diverse resistance mechanisms, including β-lactamase production, efflux pump overexpression, and target modification, enabling them to withstand multiple antibiotic classes, such as β-lactams, fluoroquinolones, and aminoglycosides.[2] The World Health Organization (WHO) has designated these species as "critical priority pathogens" requiring urgent discovery of new therapeutic agents.[3]

Despite continuous pharmaceutical research, the antibiotic development pipeline remains stagnant, with most new approvals in recent decades being structural modifications of existing scaffolds rather than truly novel compounds.[4] Plant-derived natural products offer promising potential as alternatives owing to their structural diversity, ecological abundance, and long history of therapeutic use.[5]

Medicinal plants are particularly rich in bioactive compounds, such as flavonoids, which have shown significant antimicrobial properties. Recent studies indicate that these phytochemicals can modulate microbial activity and contribute to host health.[6]

In particular, African medicinal plants widely applied in ethnomedicine for the treatment of infectious diseases remain underexplored for their antimicrobial potential in modern drug discovery.[7,8] Advances in computational biology now enable high-throughput *in silico* screening of natural products against validated microbial targets, integrating techniques such as molecular docking, pharmacokinetic (absorption, distribution, metabolism, excretion, and toxicity [ADMET]) profiling, and molecular dynamics (MD) simulations.[9,10] This approach is well-suited for identifying "dual-action" compounds capable of exerting direct antibacterial activity while simultaneously modulating bacterial virulence factors, including quorum sensing (QS) and biofilm formation.[11,12]

Targeting QS systems, such as *P. aeruginosa* LasR and the universal LuxS/autoinducer-2 signaling pathway, offers a potential strategy to attenuate pathogenicity without applying direct selective pressure, thereby potentially reducing resistance emergence.[13,14] Several classes of plant-derived compounds, including flavonoids, terpenoids, and coumarins, have demonstrated both QS inhibition and direct interference with bacterial enzymes such as DNA gyrase and β-lactamases.[15,16]

Given the rich yet underutilized phytochemical diversity of African flora, this study aims to computationally evaluate bioactive compounds from 10 ethnomedicinal plants for their dual-action potential against MDR Gram-negative pathogens.[17] Specifically, molecular docking was used to identify promising phytochemicals capable of inhibiting bacterial enzymes and QS targets, followed by ADMET prediction to assess their drug-likeness and potential safety profiles.

## 2. Materials and methods

### 2.1. Selection of medicinal plants and phytochemicals

Table 1 lists the scientific names, families, and selected phytochemicals of 10 African medicinal plants chosen for their ethnomedicinal relevance, documented antimicrobial activity, and/or QS inhibitory potential, as reported in previous ethnobotanical and phytochemical studies.[7,8] Major bioactive compounds from each plant were identified via literature mining and retrieved in Structure Data File format from the PubChem database (https://pubchem.ncbi.nlm.nih.gov/, accessed on August 5, 2025).

### 2.2. Protein structure retrieval and preparation

Crystal structures of bacterial protein targets associated with virulence and antimicrobial resistance were retrieved from the RCSB Protein Data Bank (PDB; https://www.rcsb.org/, accessed on August 5, 2025) in the Biological Assembly 1 format. The selected targets included:

(i) LasR QS regulator from *P. aeruginosa* (PDB ID: 2UV0)
(ii) AcrB efflux pump transporter from *E. coli* (PDB ID: 5NC5)
(iii) DNA gyrase subunit B from *E. coli* (PDB ID: 6F86)
(iv) TEM-1 β-lactamase from *E. coli* (PDB ID: 1BTL)

Protein preprocessing was performed using UCSF Chimera Classic version 1.16 (UCSF, USA)[18] to eliminate crystallographic artifacts (e.g., designed ankyrin repeat proteins, sulfate ion, hydrogen bonded moieties [OH···N], and cyclotryptophan-(D)-tryptophan fragments), detergents, and solvent molecules, followed by protonation at pH 7.0 using Dock Prep (Resource for Biocomputing, Visualization, and Informatics (RBVI), University of California San Francisco, USA) and geometry optimization using the Amber force field. Chain selection and correction of alternate conformations were carried out where applicable. Non-standard residues, such as selenomethionine (MSE), were converted to methionine (MET).

Protein structure preprocessing was carried out using UCSF Chimera Classic version 1.16 (Resource for Biocomputing, Visualization, and Informatics, University of California, San Francisco, USA) to eliminate

**Table 1. African medicinal plants and their selected phytochemicals**

| Plant (scientific name) | Family | Selected phytochemical | PubChem CID | Class |
|---|---|---|---|---|
| *Ocimum gratissimum* | Lamiaceae | Eugenol | 3314 | Phenylpropanoid |
| *Moringa oleifera* | Moringaceae | Quercetin | 5280343 | Flavonoid |
| *Vernonia amygdalina* | Asteraceae | Kaempferol | 5280863 | Flavonoid |
| *Tithonia diversifolia* | Asteraceae | Luteolin | 5280445 | Flavonoid |
| *Garcinia kola* | Clusiaceae | Catechin | 9064 | Flavan-3-ol |
| *Citrus aurantifolia* | Rutaceae | Naringenin | 932 | Flavanone |
| *Terminalia catappa* | Combretaceae | Ellagic acid | 5281855 | Polyphenol |
| *Ficus exasperata* | Moraceae | Gallic acid | 370 | Phenolic acid |
| *Newbouldia laevis* | Bignoniaceae | Rutin | 5280805 | Flavonoid glycoside |
| *Clerodendrum volubile* | Lamiaceae | Apigenin | 5280443 | Flavonoid |

Abbreviation: CID: Compound ID.

crystallographic artifacts, including designed ankyrin repeat proteins (DARPins), sulfate ions, hydrogen-bonded moieties (OH···N), and cyclotryptophan-(D)-tryptophan fragments.

Each prepared protein was imported into PyRx version 0.9.8 (Scripps Research Institute, USA)[19] as a macromolecule and converted to PDBQT format for docking. A blind docking protocol was applied to span the entire protein surface, ensuring that all potential binding sites were explored.

The stereochemical quality of all prepared proteins was validated using the Ramachandran plot (RamPlot) server (https://www.ramplot.in/),[20] which generated two- and three-dimensional Ramachandran plots. Residue distributions in favored and allowed regions were used to confirm the structural reliability before docking.

### 2.3. Ligand preparation

Ligands were retrieved from PubChem in Structure Data File format and processed using Open Babel version 3.1.1 (Open Babel Team, USA) integrated within PyRx version 0.9.8.[21] The workflow included conversion to three-dimensional structures, energy minimization using the universal force field, and conversion to PDBQT format for compatibility using AutoDock Vina (Scripps Research Institute, USA).

### 2.4. Molecular docking

Molecular docking was carried out using AutoDock Vina version 1.1.2 integrated within PyRx version 0.9.8.[22] Blind docking grids were set to span the entire protein structure. For each ligand–protein pair, multiple conformations were generated and ranked based on binding affinity (kcal/mol).

The top-ranked docking poses were visualized using BIOVIA Discovery Studio Visualizer version 21.1.0.20298 (Dassault Systèmes, USA) and LigPlot+ version 2.2 (European Bioinformatics Institute (EMBL-EBI), United Kingdom), in which hydrogen bonds, π–π stacking, hydrophobic interactions, and other non-covalent interactions were analyzed.

### 2.5. ADMET and drug-likeness prediction

The highest-affinity phytochemicals for each protein target were subjected to *in silico* pharmacokinetic and toxicity prediction using:

(i) SwissADME (http://www.swissadme.ch/, accessed on August 6, 2025) to evaluate Lipinski's rule of five, water solubility, gastrointestinal (GI) absorption, and blood–brain barrier permeability.[10]
(ii) pkCSM (http://biosig.unimelb.edu.au/pkcsm/, accessed on August 6, 2025) to predict metabolic and excretion profiling.
(iii) ProTox-II (https://tox-new.charite.de/protox_II, accessed on August 6, 2025) for oral toxicity classification and median lethal dose ($LD_{50}$) prediction.

No MD simulations were conducted in this study; instead, molecular docking and ADMET profiling were used as the primary computational screening approach.

## 3. Results and discussion

### 3.1. Molecular docking analysis

Molecular docking revealed strong binding affinities between the selected phytochemicals and key bacterial resistance and virulence proteins, as shown in Table 2. Protein–ligand interactions were visualized using BIOVIA Discovery Studio Visualizer.[23] Structural validation was performed using the RamPlot server. ADMET and drug-likeness predictions were carried out using SwissADME and ProTox-II, respectively.

To better understand the molecular basis of these binding affinities, the top-scoring complexes were subjected to detailed residue-level interaction analysis, highlighting hydrogen bonds, van der Waals interactions, and π-related interactions.

### *3.1.1. Interaction studies*

Protein–ligand interactions of the top-scoring complexes were analyzed in BIOVIA Discovery Studio Visualizer version 21.1. The most favorable complexes were selected for detailed analysis based on docking affinities: CID 5280445 with 1BTL (−8.3 kcal/mol), CID 5280445 with 2UV0 (−10.8 kcal/mol), CID 5280805 with 5NC5 chain A (−9.5 kcal/mol), and CID 5281855 with 6F86 (−8.3 kcal/mol). These ligands were chosen as representative inhibitors, as they demonstrated the strongest binding to their respective targets. Table 3 provides residue-level interaction details for each protein–ligand complex, including specific residues involved in hydrogen bonding, van der Waals interactions, π interactions, and unfavorable interactions.

In the 1BTL-CID 5280445 complex, the ligand formed a hydrogen-bonding network with ASN132, SER235, and ARG244, anchoring it within the active site. Van der Waals interactions with SER70, SER130, PRO167, LYS234, GLY236, and ALA237 contributed to structural

**Table 2. Summary of protein–ligand interactions for top-scoring complexes**

| Protein (PDB ID) | Ligand (CID) | Binding affinity (kcal/mol) | Key interacting residues | Interaction types |
|---|---|---|---|---|
| 1BTL (*Escherichia coli*) | 5280445 | −8.3 | ASN132, SER235, ARG244 | Hydrogen bonds |
| | | | SER70, SER130, PRO167, LYS234, GLY236, ALA237 | Van der Waals |
| | | | TYR105 | π–π stacking |
| | | | ARG244 | π–cation, donor–donor (unfavorable) |
| 2UV0 (*Pseudomonas sp.*) | 5280445 | −10.8 | SER80, ASP123, LYS173 | Hydrogen bonds |
| | | | GLN81, PRO124, LEU172, GLY174, TYR176 | Van der Waals |
| | | | PHE175, LEU178 | π–alkyl |
| | | | HIS177 | Donor–donor (unfavorable) |
| 6F86 (*Escherichia coli*) | 5281855 | −8.3 | GLU274, LYS305, TYR309 | Hydrogen bonds |
| | | | THR271, ALA273, LEU308 | Van der Waals |
| | | | PHE310 | π–π stacking |
| | | | GLY272 | amide–π |
| | | | GLU274 | π–anion |
| | | | TYR309 | π–donor, hydrogen bond |
| 5NC5 chain A (*Escherichia coli AcrBZ*) | 5280805 | −9.5 | ASN100, ASP153 | Hydrogen bonds |
| | | | GLY72, ILE101, VAL155 | Van der Waals |
| | | | PHE102, LEU150 | π–alkyl |
| | | | - | Fewer stabilizing interactions in the pump-associated complex; donor–donor clashes present |

Abbreviations: CID: Compound ID; PBD: Protein Data Bank.

**Table 3. Summary of binding affinities and interaction types for selected protein–ligand complexes**

| Protein (PDB ID) | Ligand (CID) | Binding affinity (kcal/mol) | No. of hydrogen bonds | Key interaction types |
|---|---|---|---|---|
| 1BTL (*Escherichia coli*) | 5280445 | −8.3 | 3 | Hydrogen bonds, van der Waals, π–π stacking, π–cation |
| 2UV0 (*Pseudomonas sp.*) | 5280445 | −10.8 | 3 | Hydrogen bonds, van der Waals, π–alkyl |
| 6F86 (*Escherichia coli*) | 5281855 | −8.3 | 3 | Hydrogen bonds, van der Waals, π–π stacking, π–anion, amide–π |
| 5NC5 chain A (*Escherichia coli* AcrBZ) | 5280805 | −9.5 | 2 | Hydrogen bonds, van der Waals, π–alkyl (pump-associated form showed reduced affinity) |

Abbreviations: CID: Compound ID; PBD: Protein Data Bank.

complementarity. TYR105 engaged in π–π stacking, while ARG244 contributed a π–cation interaction, partially offsetting one unfavorable donor–donor clash. This balanced network of hydrogen bonds, van der Waals forces, and π-related interactions resulted in moderate to strong binding stability.

The 2UV0–CID 5280445 (Figure 1) exhibited the strongest binding affinity among all proteins. Hydrogen bonds with SER80, ASP123, and LYS173 provided strong directional stabilization. Van der Waals interactions with GLN81, PRO124, LEU172, GLY174, and TYR176 promoted tight ligand accommodation. π–alkyl stabilization with PHE175 and LEU178 added hydrophobic reinforcement, while a donor–donor clash with HIS177 was present but outweighed by favorable interactions. This cooperative network of polar and hydrophobic interactions explains the exceptionally high affinity observed.

While hydrogen bonding and electrostatic contacts contribute to initial stabilization, hydrophobic interactions play a crucial role in ligand accommodation and binding pocket complementarity, highlighting the need for a dedicated analysis.

Binding was stabilized by hydrogen bonds with GLU274, LYS305, and TYR309, complemented by van der Waals interactions with THR271, ALA273, and LEU308. Aromatic residues made critical contributions: PHE310 formed π–π stacking, GLY272 participated in amide–π interactions, and GLU274 engaged in a π–anion contact. TYR309 contributed a π–donor hydrogen bond, reinforcing complex stability. The diverse range of polar and aromatic interactions highlights the chemical complementarity between the ligand and the binding pocket.

Hydrogen bonds with ASN100 and ASP153 anchored the ligand within the binding site, supported by van der Waals interactions with GLY72, ILE101, and VAL155. π–alkyl interactions with PHE102 and LEU150 provided additional stabilization. In contrast, when chain A was docked with the efflux pump, the affinity decreased and unfavorable donor–donor interactions emerged, indicating that pump association introduces steric hindrance and reduces effective ligand accommodation. Thus, the isolated chain A environment was more favorable for ligand binding.

Across all proteins, phytochemical inhibition was mediated by a synergistic balance of hydrogen bonding, van der Waals stabilization, and $\pi$ interactions. The strongest inhibition was observed for 2UV0 with CID 5280445 (−10.8 kcal/mol), reflecting a highly complementary binding environment. 5NC5 chain A with CID 5280805 (−9.5 kcal/mol) also exhibited strong inhibition, although affinity decreased in pump-associated forms, highlighting the effect of accessory proteins on ligand accessibility. Both 1BTL and 6F86 complexes demonstrated moderate affinities (−8.3 kcal/mol each) but were stabilized by diverse polar and aromatic interactions, as shown in Figures 1-4. Together, these findings confirm that the selected phytochemicals formed stable binding networks within their target proteins, supporting their potential as effective inhibitors.

To further elucidate the role of non-polar stabilization, a dedicated hydrophobic interaction analysis was performed. These findings, including hydrophobic residue mapping, interaction profiles, and surface visualizations, are discussed in the following section.

### 3.2. Hydrophobic interaction analysis

Hydrophobic interactions were further examined to evaluate their contribution to ligand stabilization and

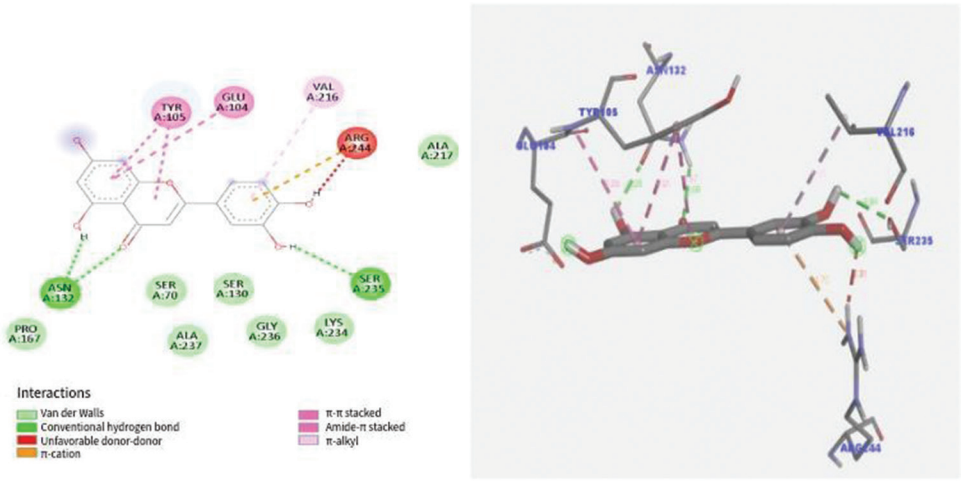


**Figure 1.** 1BTL (*Escherichia coli*)–CID 5280445 complex (−8.3 kcal/mol)

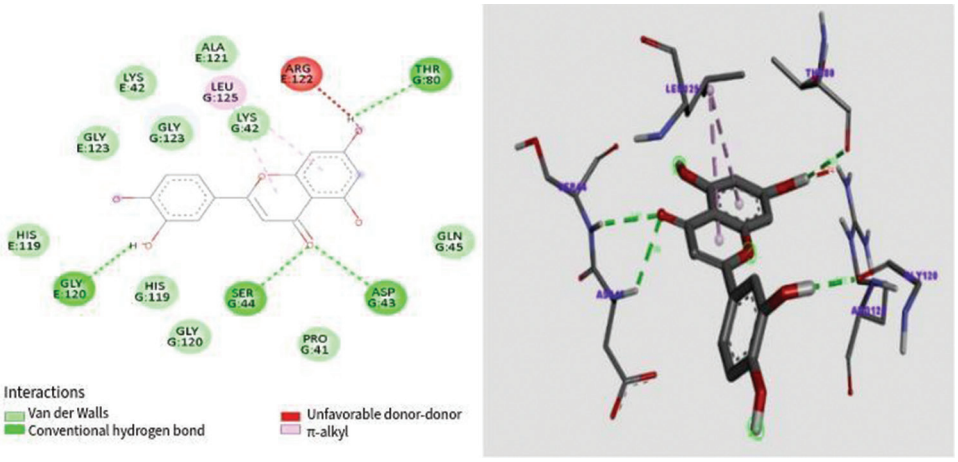


**Figure 2.** 2UV0 (*Pseudomonas sp.*)–CID 5280445 complex (−10.8 kcal/mol)

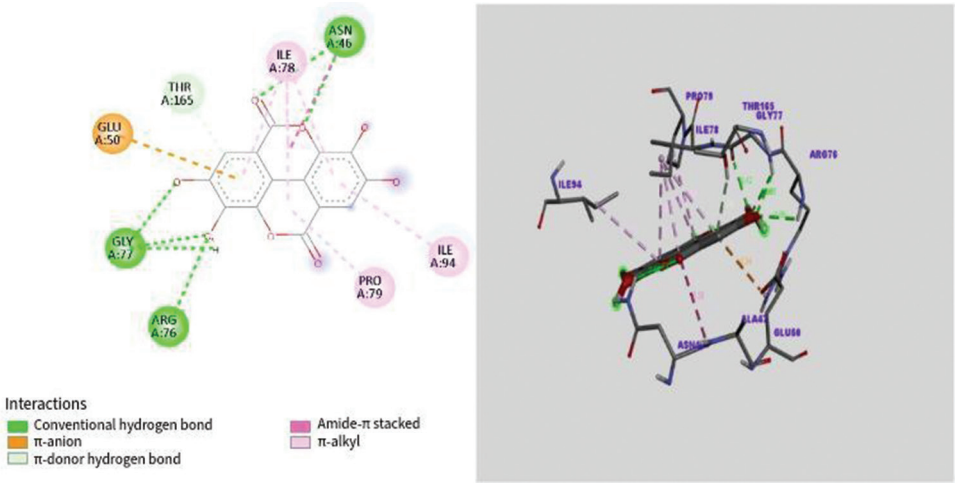


**Figure 3.** 6F86 (*Escherichia coli*)–CID 5281855 complex (−8.3 kcal/mol)

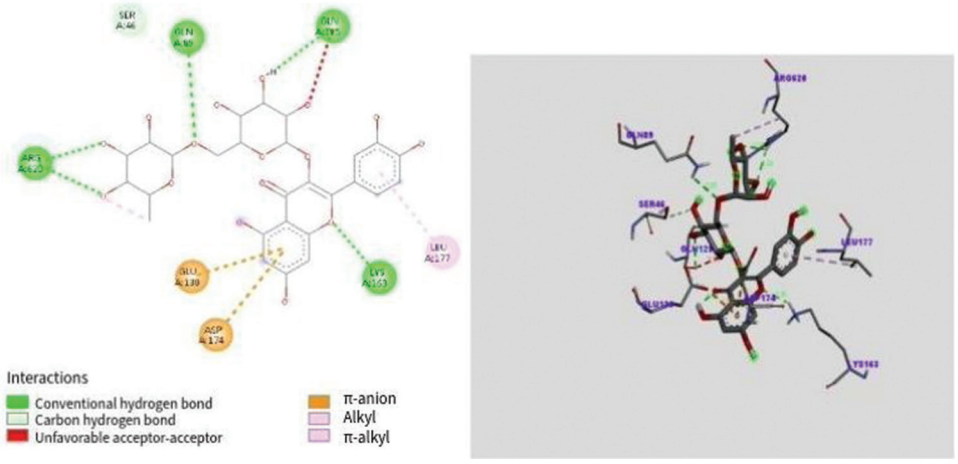


**Figure 4.** 5NC5 Chain A (*Escherichia coli* AcrBZ)–CID 5280805 complex (−9.5 kcal/mol)

solvent exclusion within the binding pockets, as shown in Table 4. Hydrophobic maps were generated using BIOVIA Discovery Studio Visualizer version 21.1, with particular attention to van der Waals interactions, π–alkyl interactions,

and aromatic stacking residues. These interactions provide a non-polar environment that complements hydrogen bonding and electrostatic stabilization, and are often critical determinants of binding affinity.

Beyond non-polar interactions, charged and polar residues contributed additional stabilization through electrostatic complementarity, synergistically enhancing overall binding affinity.

### 3.3. Per-protein hydrophobic mapping

Figure 5A-D illustrates the hydrophobic mapping of ligand–protein complexes.

For the 1BTL–CID 5280445 complex (−8.3 kcal/mol; Figure 5A), hydrophobic stabilization was mediated by van der Waals interactions with SER70, SER130, PRO167, LYS234, GLY236, and ALA237, creating a compact non-polar microenvironment. TYR105 provided π–π stacking with the ligand's aromatic ring, while ARG244 engaged in π–cation stabilization.

For the 2UV0–CID 5280445 complex (−10.8 kcal/mol; Figure 5B), the most extensive hydrophobic network was observed, involving van der Waals interactions with GLN81, PRO124, LEU172, GLY174, and TYR176. π–alkyl interactions with PHE175 and LEU178 further shielded the ligand from solvent exposure, consistent with the highest observed affinity.

For the 6F86–CID 5281855 complex (−8.3 kcal/mol; Figure 5C), non-polar stabilization was mediated by THR271, ALA273, and LEU308. In addition, aromatic residues PHE310 and TYR309 contributed to π–π stacking

**Table 4. Hydrophobic interactions observed in the selected protein–ligand complexes**

| Protein (PDB ID) | Ligand (CID) | Binding affinity (kcal/mol) | Key hydrophobic residues | Interaction types |
|---|---|---|---|---|
| 1BTL (*Escherichia coli*) | 5280445 | −8.3 | SER70, SER130, PRO167, LYS234, GLY236, ALA237, TYR105, ARG244 | Van der Waals, π–π stacking, π–cation |
| 2UV0 (*Pseudomonas sp.*) | 5280445 | −10.8 | GLN81, PRO124, LEU172, GLY174, TYR176, PHE175, LEU178 | Van der Waals, π–alkyl |
| 6F86 (*Escherichia coli*) | 5281855 | −8.3 | THR271, ALA273, LEU308, PHE310, TYR309 | Van der Waals, π–π stacking, π–donor |
| 5NC5 chain A (*Escherichia coli AcrBZ*) | 5280805 | −9.5 | GLY72, ILE101, VAL155, PHE102, LEU150 | Van der Waals, π–alkyl |

Abbreviations: CID: Compound ID; PBD: Protein Data Bank.

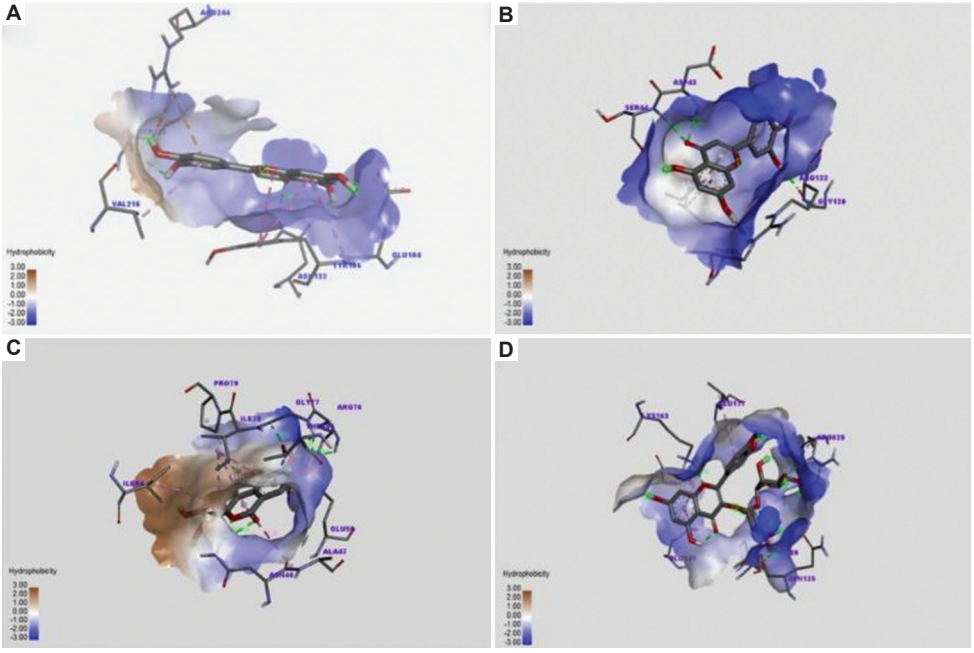


**Figure 5.** Hydrophobic surface mapping of ligand–protein complexes: (A) 1BTL–CID 5280445 (−8.3 kcal/mol), (B) 2UV0–CID 5280445 (−10.8 kcal/mol), (C) 6F86–CID 5281855 (−8.3 kcal/mol), and (D) 5NC5 chain A–CID 5280805 (−9.5 kcal/mol)
Abbreviation: CID: Compound ID.

and π–donor hydrogen bonding, respectively, effectively positioning the ligand within a hydrophobic cavity

For the 5NC5 chain A–CID 5280805 complex (–9.5 kcal/mol; Figure 5D), van der Waals interactions with GLY72, ILE101, and VAL155 provided a hydrophobic framework, supplemented by π–alkyl stabilization from PHE102 and LEU150. The loss of several of these hydrophobic interactions in the pump-associated complex correlated with reduced affinity.

Hydrophobic stabilization was found to be a consistent determinant of binding strength across all studied complexes. The 2UV0–CID 5280445 complex exhibited the densest hydrophobic packing, consistent with its strongest binding affinity (–10.8 kcal/mol). The 5NC5 chain A–CID 5280805 complex also showed significant hydrophobic reinforcement (–9.5 kcal/mol), although steric effects in the pump-associated form led to reduced binding stability. Both 1BTL and 6F86 demonstrated moderate hydrophobic contributions, with stabilization strongly dependent on key aromatic residues (TYR105 and PHE310/TYR309, respectively). These findings underscore the crucial role of hydrophobic complementarity in determining phytochemical-mediated inhibition of bacterial target proteins.

### 3.4. Ionizability and electrostatic interaction analysis

Electrostatic complementarity between ionizable residues in the protein and the polar or charged groups of the ligands was analyzed to evaluate their contribution to binding stability. Charged residues frequently stabilized the ligand through salt bridges, ionic interactions, or charge-assisted hydrogen bonds. These interactions helped orient the ligands within the binding pocket and synergistically enhanced affinity in cooperation with hydrophobic packing, as shown in Figure 6A-D.

For the 1BTL–CID 5280445 complex (–8.3 kcal/mol; Figure 6A), electrostatic stabilization was mediated by ARG244, which formed a charge-assisted hydrogen bond with the ligand's polar group while also engaging in π–cation interactions. The dual role of this residue highlights its importance in anchoring the ligand despite the presence of a donor–donor clash.

For the 2UV0–CID 5280445 complex (–10.8 kcal/mol; Figure 6B), strong ionic contributions were observed from ASP123 and LYS173, which formed polar hydrogen bonds with the ligand's functional groups. These residues generated a stabilizing electrostatic environment that complemented the extensive hydrophobic pocket, thereby explaining the exceptionally high affinity of this complex.

For the 6F86–CID 5281855 complex (–8.3 kcal/mol; Figure 6C), electrostatic interactions were primarily mediated by GLU274 and LYS305. GLU274 provided a π–anion interaction with the ligand's aromatic group, while LYS305 stabilized the binding through a conventional

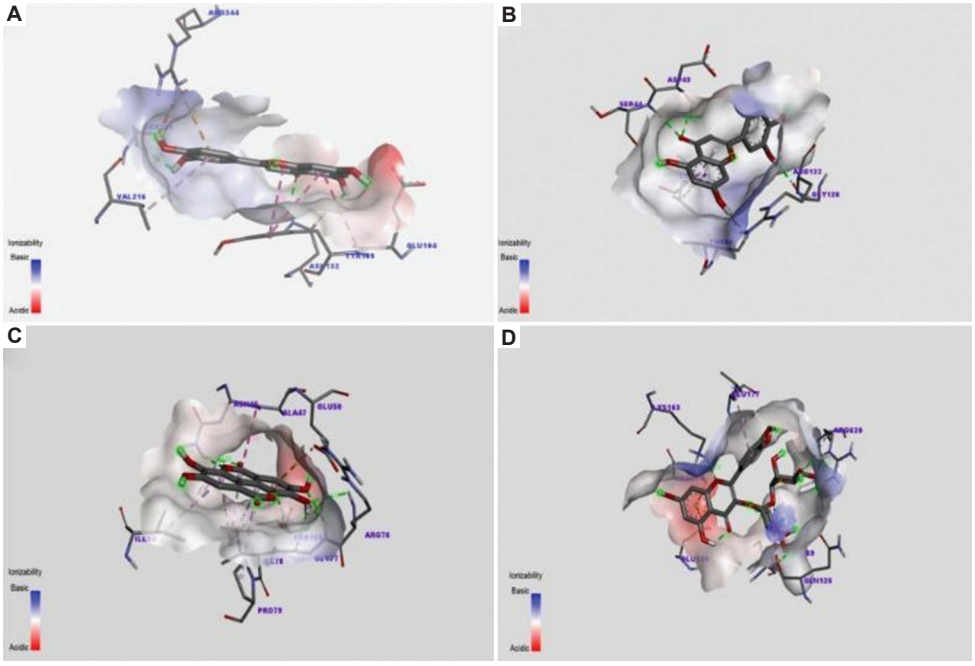


**Figure 6.** Electrostatic interaction mapping of ligand–protein complexes: (A) 1BTL–CID 5280445 (–8.3 kcal/mol), (B) 2UV0–CID 5280445 (–10.8 kcal/mol), (C) 6F86–CID 5281855 (–8.3 kcal/mol), and (D) 5NC5 chain A–CID 5280805 (–9.5 kcal/mol)
Abbreviation: CID: Compound ID.

hydrogen bond. Together, these ionizable residues balanced the polar–non-polar interactions within the binding cavity.

However, for the 5NC5 chain A–CID 5280805 complex (−9.5 kcal/mol; Figure 6D), electrostatic interactions were comparatively weaker, limited to polar interactions with ASN100 and ASP153. While not as extensive as those in the 2UV0–CID 5280445 complex, these residues nevertheless provided key anchoring points for the ligand within the AcrBZ chain A binding pocket. In the pump-associated form, steric interference reduced both hydrophobic and electrostatic contacts, resulting in decreased binding stability.

Electrostatic interactions played a supportive yet essential role in stabilizing the docked phytochemicals. Complexes with higher affinity (2UV0 and 5NC5 chain A) displayed well-distributed ionic interactions involving both acidic (ASP, GLU) and basic (ARG, LYS) residues, which complemented the dense hydrophobic packing. In contrast, complexes with moderate affinity (1BTL and 6F86) exhibited fewer electrostatic interactions, relying more heavily on aromatic and van der Waals interactions, as presented in Table 5. These findings indicate that ionizability and charge complementarity are critical determinants in fine-tuning phytochemical inhibition of bacterial targets.

To further assess how ligand positioning and burial within the binding pocket influence binding strength, solvent-accessible surface (SAS) analyses were conducted.

### 3.5. Solvent-accessible surface analysis

To assess the degree of ligand burial within the protein cavities, SAS areas were calculated and visualized using BIOVIA Discovery Studio Visualizer v21.1. This analysis provides insights into the extent of ligand exposure to solvent versus its encapsulation within the binding pocket. A reduced SAS typically indicates deeper ligand insertion and stronger hydrophobic stabilization, whereas higher SAS values suggest partial solvent exposure and weaker binding, as illustrated in Figure 7A-D.

For the 1BTL–CID 5280445 complex (−8.3 kcal/mol; Figure 7A), the ligand was moderately buried within the binding pocket, with aromatic moieties partially shielded by TYR105 and ARG244. SAS mapping revealed that while hydrophobic residues contributed to partial encapsulation, some solvent exposure remained, consistent with its intermediate binding affinity.

For the 2UV0–CID 5280445 complex (−10.8 kcal/mol; Figure 7B), the ligand displayed the deepest insertion among all complexes, with SAS mapping revealing near-complete encapsulation by hydrophobic residues GLN81, PRO124, LEU172, and PHE175. This low solvent accessibility correlated with the highest binding affinity, reflecting efficient desolvation and tight packing within the non-polar pocket.

For the 6F86–CID 5281855 complex (−8.3 kcal/mol; Figure 7C), the ligand was partially embedded, with SAS analysis showing moderate burial. While PHE310 and TYR309 shielded the aromatic ring system, other portions of the ligand remained solvent-exposed. This balance between burial and exposure likely contributed to the moderate binding affinity of this complex.

For the 5NC5 chain A–CID 5280805 complex (−9.5 kcal/mol; Figure 7D), the ligand exhibited strong burial within the chain A pocket, with van der Waals and π–alkyl interactions reducing solvent exposure. SAS visualization confirmed that the isolated chain A complex had greater encapsulation compared with the pump-associated form, where steric interference increased solvent accessibility and reduced affinity.

Solvent-accessible surface analysis confirmed that ligand burial strongly correlated with binding affinity. The 2UV0–CID 5280445 complex demonstrated the lowest solvent exposure, consistent with its highest affinity (−10.8 kcal/mol). The 5NC5 chain A–CID 5280805 complex also exhibited strong burial, although this effect was reduced when docked with the efflux pump. In contrast, the 1BTL and 6F86 complexes showed partial solvent exposure,

**Table 5. Ionizable residues and electrostatic interactions in the selected protein–ligand complexes**

| Protein (PDB ID) | Ligand (CID) | Binding affinity (kcal/mol) | Key ionizable residues | Electrostatic interaction types |
|---|---|---|---|---|
| 1BTL (*Escherichia coli*) | 5280445 | −8.3 | ARG244 | Charge-assisted hydrogen bond, π–cation, donor–donor clash |
| 2UV0 (*Pseudomonas sp.*) | 5280445 | −10.8 | ASP123, LYS173 | Ionic hydrogen bonds, salt bridge stabilization |
| 6F86 (*Escherichia coli*) | 5281855 | −8.3 | GLU274, LYS305, TYR309 | π–anion (GLU274), charge-assisted hydrogen bond (LYS305), polar hydrogen bond donor (TYR309) |
| 5NC5 chain A (*Escherichia coli* AcrBZ) | 5280805 | −9.5 | ASN100, ASP153 | Polar hydrogen bonds (acidic/basic complementarity) |

Abbreviations: CID: Compound ID; PBD: Protein Data Bank.

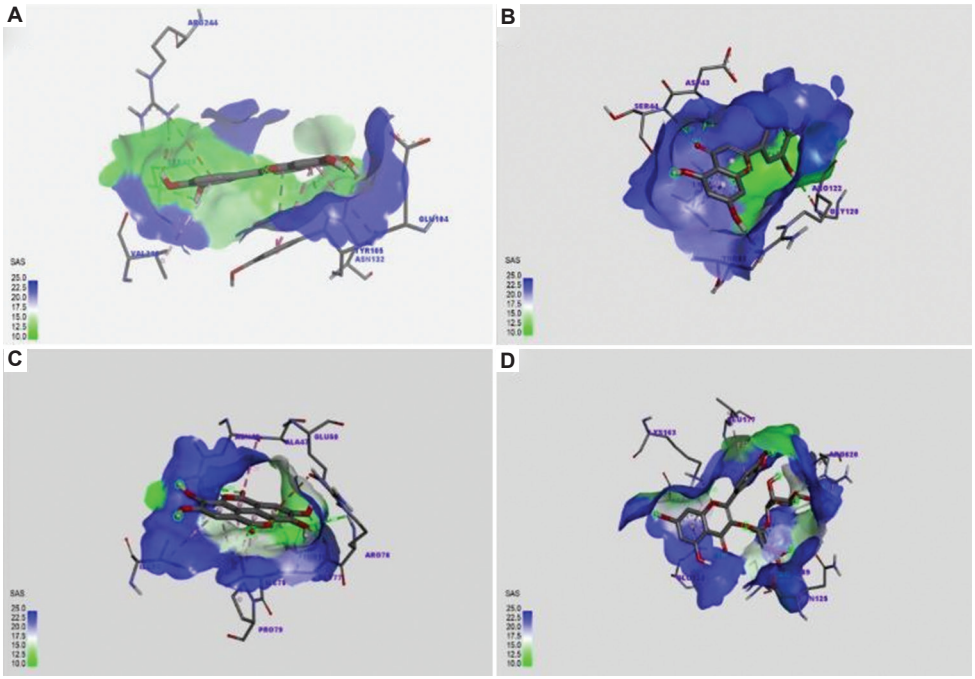


**Figure 7.** Solvent-accessible surface mapping of ligand–protein complexes: (A) 1BTL–CID 5280445 (−8.3 kcal/mol), (B) 2UV0–CID 5280445 (−10.8 kcal/mol), (C) 6F86–CID 5281855 (−8.3 kcal/mol), and (D) 5NC5 chain A–CID 5280805 (−9.5 kcal/mol)
Abbreviations: CID: Compound ID; SAS: Solvent-accessible surface analysis.

aligning with their moderate binding affinities. Together, these findings highlight that reduced SAS (greater ligand encapsulation) serves as a key determinant of phytochemical-mediated protein inhibition.

Complementing the solvent exposure data, hydrogen-bond length analysis provided insights into the precise geometries of hydrogen bonds and other stabilizing contacts that underpin complex stability.

### 3.6. Bond length analysis and its impact on interaction strength

#### *3.6.1. 1BTL–ligand complex*

The docking analysis of 1BTL with the ligand (CID 5280445) revealed hydrogen bonds with ASN132, SER235, and ARG244, with bond lengths ranging from 2.7 to 2.9 Å, consistent with strong stabilizing interactions. Van der Waals interactions with SER70, SER130, PRO167, LYS234, GLY236, and ALA237 supported close packing, while π–π stacking with TYR105 and π–cation interaction with ARG244 enhanced binding affinity. Despite a donor–donor repulsion observed with ARG244, the unfavorable contact occurred at a relatively longer bond length (>3.1 Å), thereby minimizing its destabilizing effect. Overall, the shorter hydrogen bond distances outweighed the penalty from unfavorable contacts.

#### *3.6.2. 2UV0–ligand complex*

In the 2UV0 complex, multiple stabilizing hydrogen bonds were observed with GLY120, GLY123, SER44, ASP43, and THR80, with bond lengths clustered around 2.8–3.0 Å, indicating stable anchoring. Van der Waals interactions with ALA121, HIS119, and PRO41, together with π–alkyl interactions (LEU125, LYS42), complemented the hydrogen bonding. An unfavorable donor–donor clash with ARG122 was detected, but its longer bond distance (approximately 3.2 Å) reduced its destabilizing contribution. Overall, the predominance of shorter hydrogen bonds and hydrophobic stabilization compensated for the repulsive contact.

#### *3.6.3. 6F86–ligand complex*

The ligand bound to 6F86 through hydrogen bonds with ASN46, GLY77, ARG76, and ILE78, exhibiting bond lengths of 2.6–2.9 Å, characteristic of strong interactions. π–anion interaction with GLU50 and amide–π stacking with PRO79 and ILE94 provided additional stabilization. A combination of π–donor hydrogen bonding and van der Waals forces further optimized the ligand's orientation. No significant unfavorable interactions were observed at short distances, making this complex one of the most stable based on its bond length profile.

#### *3.6.4. 5NC5 (chain A, B, and C)–ligand complexes*

In 5NC5, the effect of the pump protein was evident when comparing the isolated chains to chain–pump complexes.

For chain A, hydrogen bond lengths averaged 2.7–2.9 Å, but the presence of an additional donor–donor clash with ARG introduced local instability. Chain B displayed hydrogen bonds with bond lengths of approximately 2.85 Å, but simultaneous acceptor–acceptor repulsions at 2.95 Å weakened stability, resulting in slightly lower binding affinity. Chain C exhibited a comparable binding affinity to chain A, although unfavorable interactions were present at shorter distances, increasing repulsive effects. Overall, the isolated chains (without pump) demonstrated shorter, more stable hydrogen bonds and hence stronger affinities than their pump-associated counterparts. The results are provided in Table 6.

### 3.7. Ramachandran plot analysis

Ramachandran plots were generated for all proteins to assess stereochemical quality and backbone conformational preferences. In these plots, residues are distributed across favorable, allowed, and disallowed regions, with additional frequency maps providing insights into the dominant secondary structure motifs.

For 1BTL (Figure 8), the standard plot showed that the majority of residues were concentrated in favorable α-helical and β-sheet regions, with very few residues occupying disallowed zones (Figure 8A). The corresponding frequency plot revealed a high density in the helical region, confirming the structural dominance of α-helices (Figure 8B). Residue-specific maps further demonstrated the expected flexibility of glycine residues and the conformational restriction of proline residues (Figure 8C), while the extended map confirmed overall stereochemical stability with minimal strain (Figure 8D). With the protein structures validated, attention was then turned to the predicted toxicity profiles of the ligands to evaluate their potential systemic risks.

Similarly, the Ramachandran plots of 2UV0 demonstrated strong clustering of residues in favorable regions, particularly within β-strand conformations (Figure 9). The frequency distribution displayed a prominent density peak in the extended β-sheet region, supporting the prevalence of this secondary structure (Figure 9B). Glycine residues exhibited broader scattering across allowed regions, reflecting their inherent flexibility, whereas proline residues remained confined to restricted zones. The extended conformational overview suggested excellent stereochemical quality, with negligible outliers (Figure 9C).

For 5NC5 (chain A), the majority of residues were distributed within favorable regions, although a small proportion appeared in disallowed zones, likely due to loop conformations (Figure 10). The frequency map indicated a mixed distribution between α-helical and β-strand regions, consistent with its composite secondary structure (Figure 10B). Glycine residues displayed a wider conformational spread, whereas proline residues occupied the expected ϕ–ψ ranges. Despite a few deviations, the extended analysis confirmed that the structure retained acceptable stereochemical quality for docking (Figure 10C).

For 6F86, the plots confirmed the highest degree of stereochemical refinement among the analyzed proteins (Figure 11). The majority of residues clustered within favorable regions, with the frequency map showing a sharp density peak in the α-helical zone, indicating the structural dominance of α-helices (Figure 11B). Glycine residues displayed broader conformational variability, while proline residues remained appropriately confined. The extended conformational analysis reinforced the overall stability of this protein, with only rare outlier residues observed (Figure 11D).

### 3.8. Toxicity prediction (ProTox analysis)

The toxicity of ligands CID 5280445, CID 5280805, and CID 5281855 was predicted using the ProTox-3.0 platform. The

**Table 6. Bond length analysis and stability assessment**

| Protein–ligand complex | Key hydrogen-bonding residues | Favorable bond lengths (Å) | Unfavorable interactions (type and length) | Stability assessment |
|---|---|---|---|---|
| 1BTL–ligand | ASN132, SER235, ARG244 | 2.7–2.9 (hydrogen bonds) | Donor–donor with ARG244 (>3.1 Å) | Stable; short hydrogen bonds outweigh weak repulsion |
| 2UV0–ligand | GLY120, GLY123, SER44, ASP43, THR80 | 2.8–3.0 (hydrogen bonds) | Donor–donor with ARG122 (~3.2 Å) | Stable; strong hydrogen-bond network compensates for minor repulsion |
| 6F86–ligand | ASN46, GLY77, ARG76, ILE78 | 2.6–2.9 (hydrogen bonds); π–anion, π–π stacking | None significant | Very stable; multiple favorable short interactions |
| 5NC5 chain A–ligand | Multiple hydrogen bonds | 2.7–2.9 (hydrogen bonds) | Donor–donor with ARG (~3.0 Å) | Stable overall, slight perturbation from clash |
| 5NC5 chain B–ligand | SER–ligand (hydrogen bond) | 2.85 (hydrogen bonds) | Acceptor–acceptor (~2.95 Å) | Less stable; repulsion weakens bond |
| 5NC5 chain C–ligand | Multiple hydrogen bonds | 2.8–3.0 (hydrogen bonds) | Short unfavorable contacts (<3.0 Å) | Moderately stable; repulsion slightly reduces affinity |

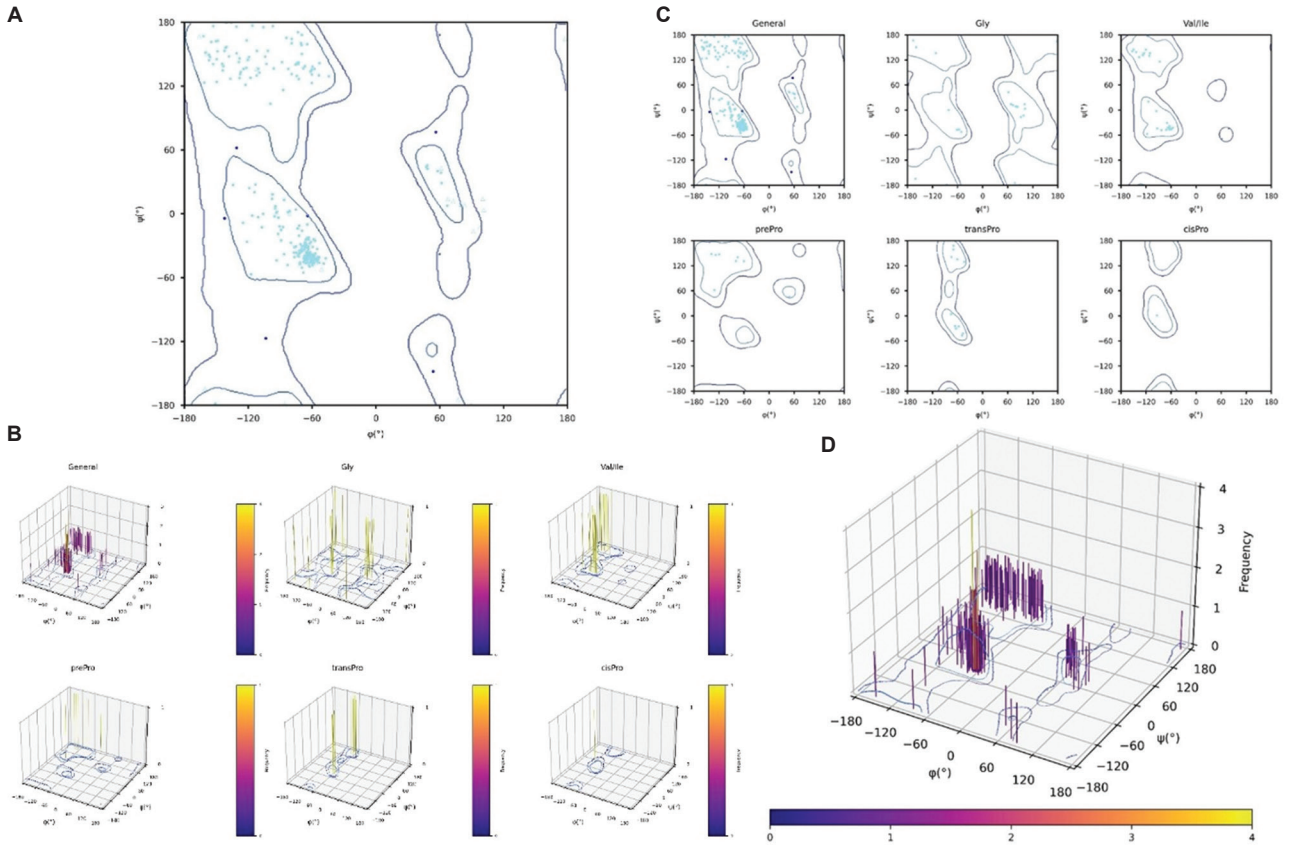


**Figure 8.** Ramachandran plot analysis. (A) Standard 2D-Ramachandran Map; (B) 3D Ramachandran bar plot frequency of torsion angles; (C) 2D Ramachandran plot (Alanine,15 amino acids; Gly; Val/Ile; pre-Pro; trans-Pro; cis-Pro); (D) Standard 3D Ramachandran bar plot frequency of torsion angles; favored (cyan), allowed (blue), disallowed regions (red).

predicted toxicological profiles encompass organ-specific toxicities, toxicity endpoints, nuclear receptor activation, stress responses, metabolic liabilities, dose distributions, and bond-level structural contributions to toxicity.

#### *3.8.1. Organ toxicity and endpoints*

Radar plots of organ toxicity revealed that all ligands were consistently predicted to be inactive for hepatotoxicity, neurotoxicity, and cardiotoxicity (Figure 12). However, nephrotoxicity and respiratory toxicity were predicted as active in all three ligands, with CID 5280805 showing the strongest nephrotoxic signal (probability: 0.77). Bar graphs of toxicity endpoints revealed compound-specific differences: CID 5280445 exhibited risks for carcinogenicity (0.68), mutagenicity (0.51), and nutritional toxicity (0.63), whereas CID 5280805 was predicted to be immunotoxic (0.98) and also showed nutritional toxicity (0.54). CID 5281855 showed an intermediate pattern with moderate immunotoxic and mutagenic predictions.

In addition to toxicity assessment, ADMET profiling was performed to evaluate pharmacokinetic behavior and overall drug-likeness properties of each phytochemical candidate.

### 3.9. Nuclear receptor and stress pathways

Analysis of nuclear receptor signaling revealed that CID 5280445 shows strong interactions with the aryl hydrocarbon receptor (0.91) and estrogen receptor (ER) pathways (Erα: 0.87; ER–ligand-binding domain: 0.95), suggesting possible endocrine-disrupting potential. In contrast, CID 5280805 and CID 5281855 displayed minimal receptor activation. Stress response predictions further identified CID 5280445 as a mitochondrial-stress liability, with strong activation of the mitochondrial membrane potential (probability: 1.0). No significant stress pathway activation was observed for CID 5280805 or CID 5281855.

#### *3.9.1. Metabolic liabilities*

Cytochrome P450 (CYP) enzyme interactions were predicted to be strongest for CID 5280445, which activated CYP1A2, CYP2C9, and CYP2C19, suggesting higher

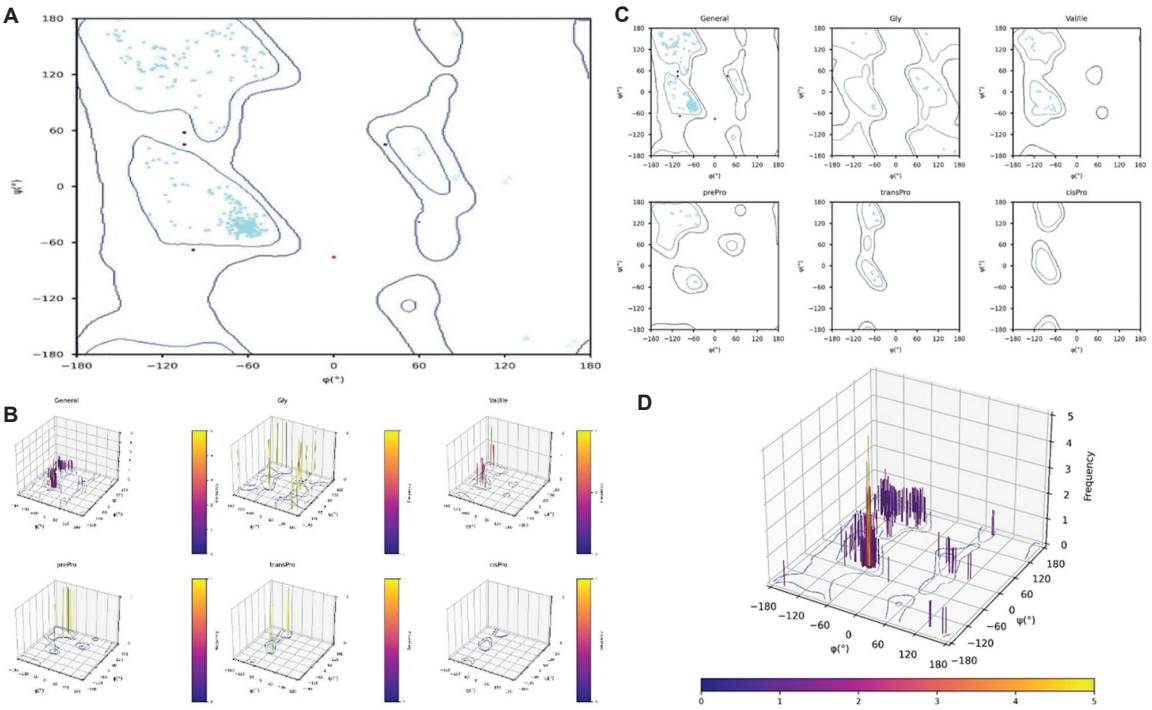


**Figure 9.** Ramachandran plot analysis. (A) Standard 2D-Ramachandran Map; (B) 3D Ramachandran bar plot frequency of torsion angles; (C) 2D Ramachandran plot (Alanine,15 amino acids; Gly; Val/Ile; pre-Pro; trans-Pro; cis-Pro); (D) Standard 3D Ramachandran bar plot frequency of torsion angles; favored (cyan), allowed (blue), disallowed regions (red).

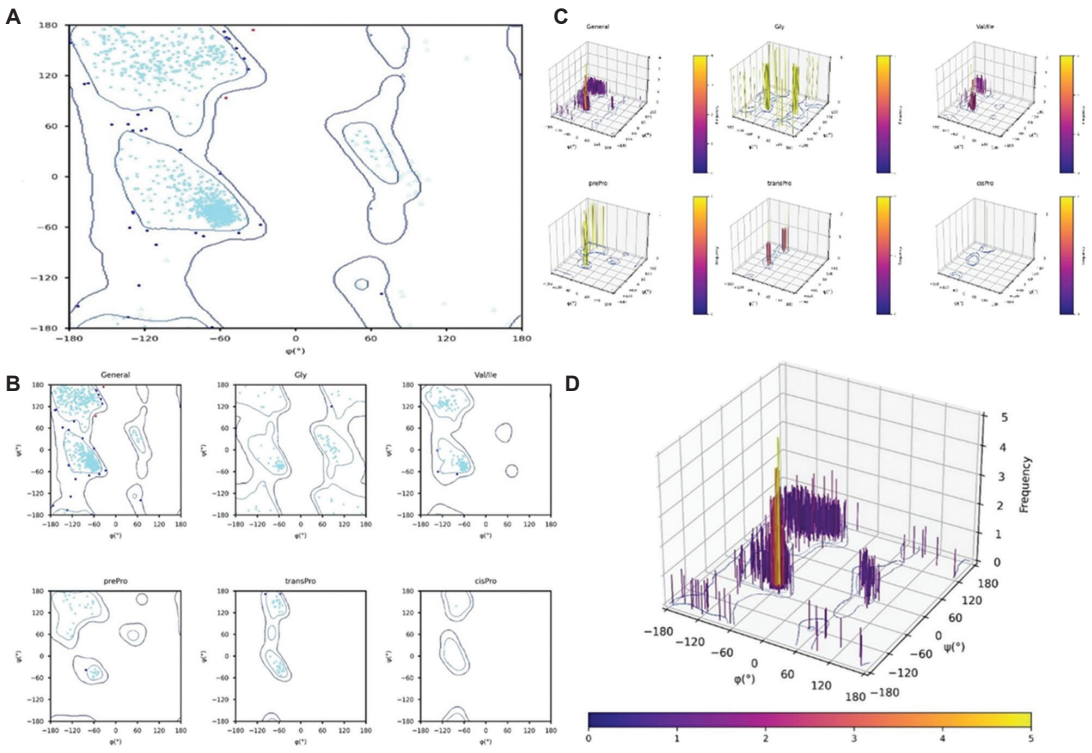


**Figure 10.** Ramachandran plot analysis. (A) Standard 2D-Ramachandran Map; (B) 3D Ramachandran bar plot frequency of torsion angles; (C) 2D Ramachandran plot (Alanine,15 amino acids; Gly; Val/Ile; pre-Pro; trans-Pro; cis-Pro); (D) Standard 3D Ramachandran bar plot frequency of torsion angles; favored (cyan), allowed (blue), disallowed regions (red).

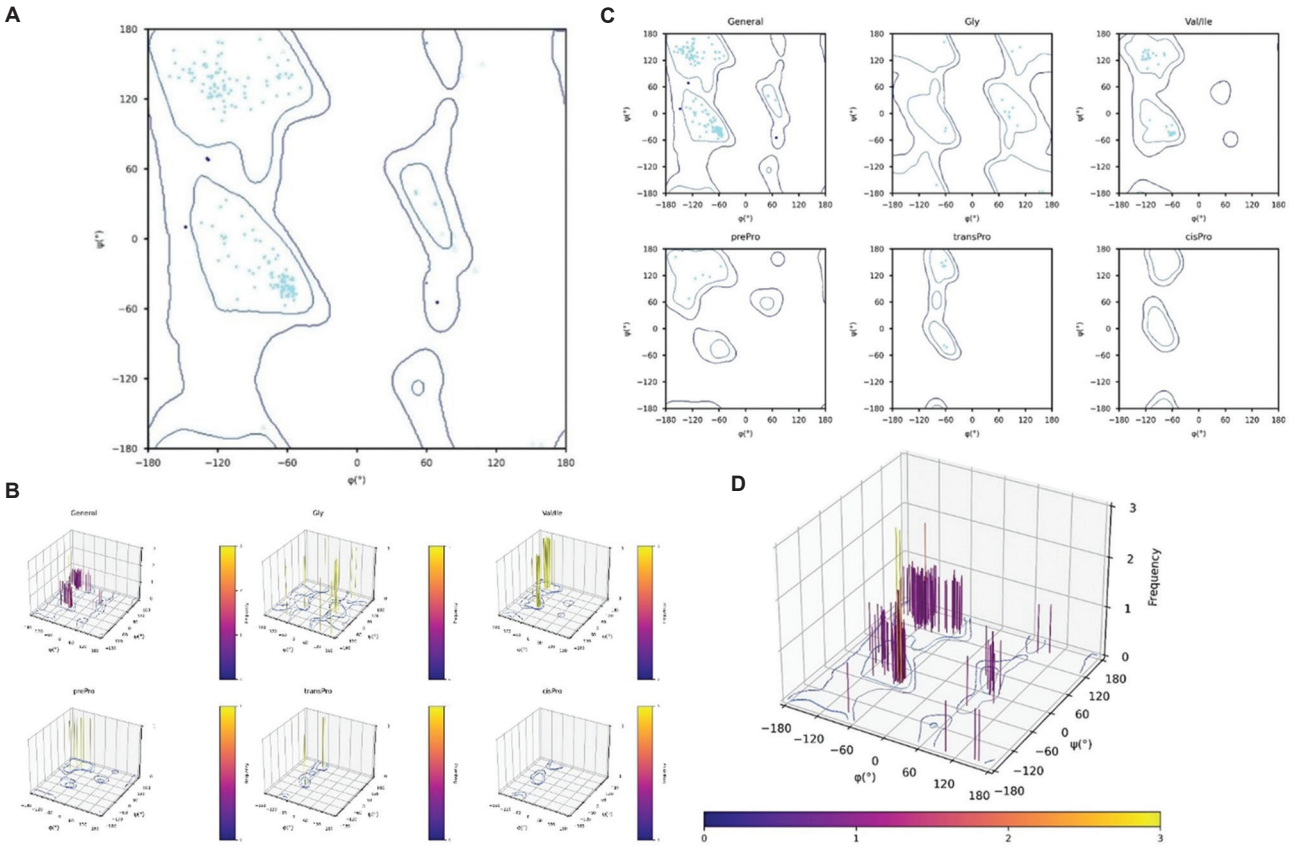


**Figure 11.** Ramachandran plot analysis. (A) Standard 2D-Ramachandran Map; (B) 3D Ramachandran bar plot frequency of torsion angles; (C) 2D Ramachandran plot (Alanine,15 amino acids; Gly; Val/Ile; pre-Pro; trans-Pro; cis-Pro); (D) Standard 3D Ramachandran bar plot frequency of torsion angles; favored (cyan), allowed (blue), disallowed regions (red).

metabolic turnover and a possible risk of drug–drug interactions. Both CID 5280805 and CID 5281855 exhibited minimal CYP450 activation, indicating comparatively safer metabolic profiles.

### *3.9.2. Dose distribution*

The dose distribution plots (Figure 13) illustrate the predicted $LD_{50}$ values and corresponding toxicity classes. CID 5280445 showed a distribution toward lower $LD_{50}$ values, indicating higher acute toxicity and reduced dosage safety margins. In contrast, CID 5280805 and CID 5281855 were associated with distributions at higher $LD_{50}$ values, reflecting comparatively lower predicted acute toxicity.

### *3.9.3. Bond distribution*

As shown in Figure 14, bond distribution graphs revealed the structural determinants underlying toxicity predictions. For CID 5280445, aromatic and heteroatomic bonds contributed prominently to toxicity endpoints, consistent with its observed receptor pathway activations and mutagenicity. In contrast, CID 5280805 and CID 5281855 displayed more balanced bond distributions, with fewer structural alerts, supporting their comparatively safer toxicity predictions. These findings highlight how molecular structure directly influences toxicity risk.

Among the three ligands, CID 5280805 demonstrated the most favorable toxicity profile, with limited active predictions beyond immunotoxicity and nutritional toxicity. CID 5281855 exhibited an intermediate profile, whereas CID 5280445 exhibited the greatest toxicological risk, with strong carcinogenic, mutagenic, metabolic, and mitochondrial stress predictions. These findings provide an early safety evaluation and support the prioritization of ligands for further *in vitro* validation.

## 3.10. ADMET analysis

The pharmacokinetic and drug-likeness properties of luteolin (CID 5280445), rutin (CID 5280805), and ellagic acid (CID 5281855) were evaluated using *in silico* ADMET profiling tools. The assessment covered absorption, distribution, metabolism, excretion, and medicinal chemistry filters, which are essential for determining drug suitability.

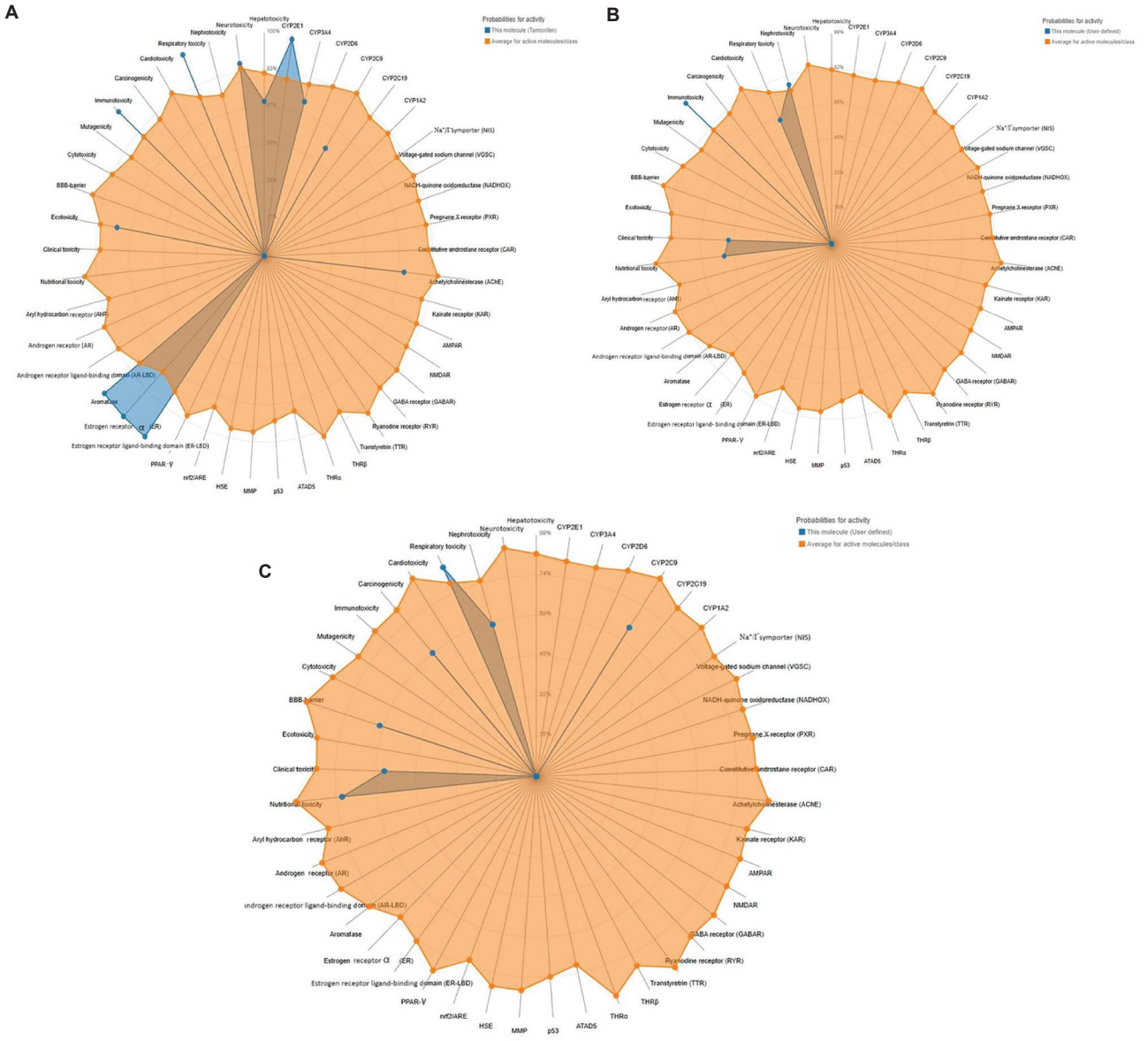


**Figure 12.** Radar plots showing comparative toxicity profiles of ligands (A) CID 5280445, (B) CID 5280805, and (C) CID 5281855 against the average reference molecule, highlighting variations in nephrotoxic and immunotoxic tendencies
Abbreviations: CID: Compound ID.

### *3.10.1. Ligand 1: Luteolin (CID 5280445)*

Luteolin ($C_{15}H_{10}O_6$; molecular weight [MW]: 286.24 g/mol) exhibited favorable physicochemical properties, including a topological polar surface area (TPSA) of 111.13 Å$^2$ and a consensus LogP of 1.73. The compound was predicted to have high GI absorption but not to cross the blood–brain barrier (BBB) and not to act as a P-glycoprotein substrate. It was predicted to inhibit CYP1A2, CYP2D6, and CYP3A4, suggesting moderate metabolic liabilities. Skin permeation was acceptable (log Kp = −6.25 cm/s).

Luteolin satisfied major drug-likeness filters (e.g., Lipinski, Ghose, Veber, Egan, and Muegge) without violations and had a bioavailability score of 0.55. Medicinal chemistry analysis flagged one pan-assay interference compound (PAINS) alert (catechol A) and one Brenk alert (catechol). Synthetic accessibility was favorable (score: 3.02). Overall, luteolin demonstrated good oral bioavailability and compliance with drug-likeness rules, although CYP inhibition and PAINS alerts should be considered.

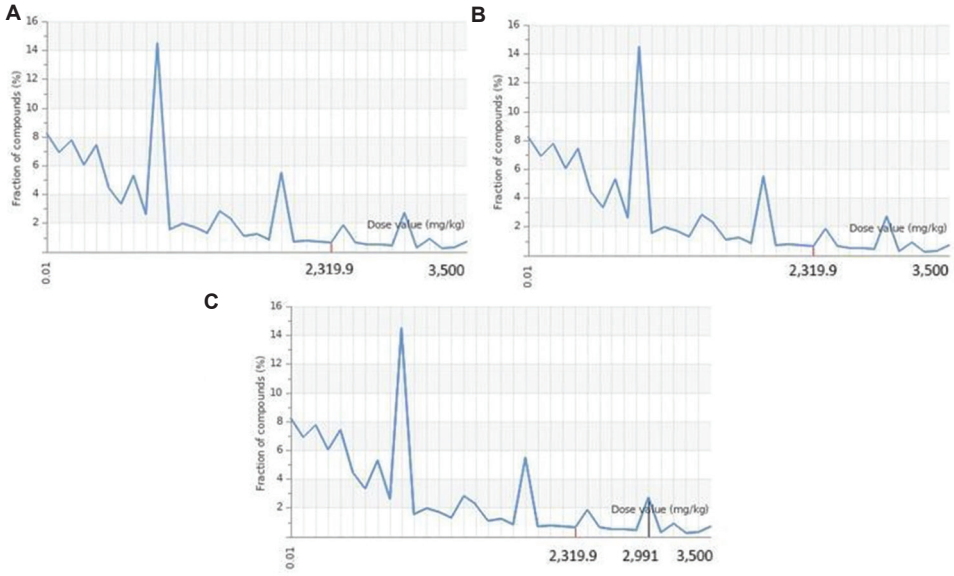


**Figure 13.** Dose distribution and $LD_{50}$ profiles of ligands (A) CID 5280445, (B) CID 5280805, and (C) CID 5281855. CID 5280445 exhibited lower $LD_{50}$, indicating higher acute toxicity, whereas CID 5280805 and CID 5281855 exhibited higher $LD_{50}$ values, suggesting lower toxicity.
Abbreviations: CID: Compound ID; $LD_{50}$: Median lethal dose.

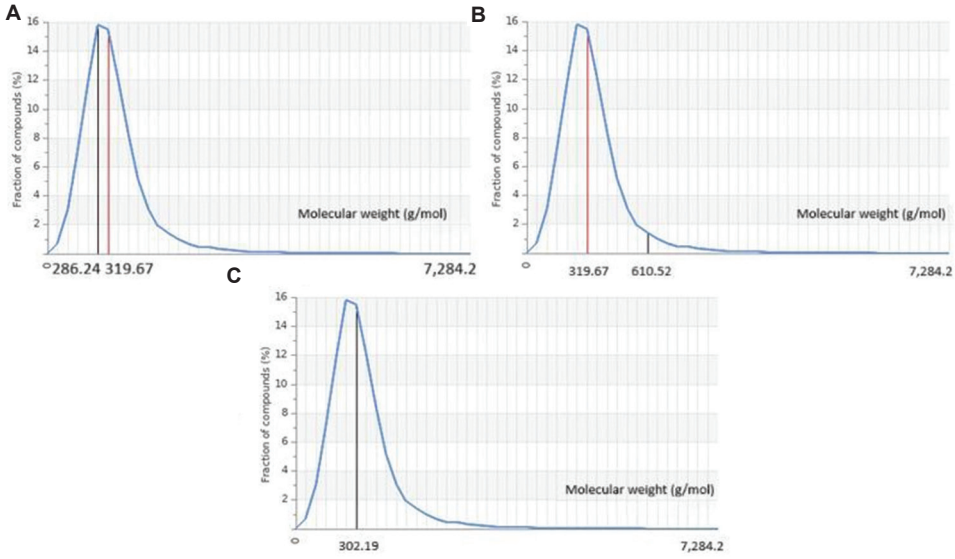


**Figure 14.** Bond distribution and structural determinants of ligands (A) CID 5280445, (B) CID 5280805, and (C) CID 5281855 toxicity. CID 5280445 exhibited higher aromatic and heteroatomic bond contributions associated with greater toxicity, whereas CID 5280805 and CID 5281855 displayed more balanced bond distributions, indicating comparatively lower toxicity risks.
Abbreviation: CID: Compound ID.

### *3.10.2. Ligand 2: Rutin (CID 5280805)*

Rutin ($C_{27}H_{30}O_{16}$; MW: 610.52 g/mol) exhibited less favorable ADMET characteristics, with a TPSA of 269.43 $Å^2$ and a consensus LogP of −1.51, indicating high polarity and low lipophilicity. It was predicted to have low GI absorption, not to cross the BBB, and to act as a P-glycoprotein substrate, suggesting efflux limitations. Unlike luteolin, this compound was not predicted to inhibit major CYP450 isoforms, thereby minimizing risks of metabolic interactions. Skin permeation was very poor (log Kp = −10.26 cm/s).

Drug-likeness evaluation revealed multiple violations: Lipinski (MW >500, excess hydrogen-bond donors/acceptors), Ghose, Egan, and Muegge. The bioavailability score was low (0.17). Medicinal chemistry filters flagged

catechol A and catechol alerts. Synthetic accessibility was poor (6.52), reflecting structural complexity. Overall, rutin demonstrated poor oral absorption and limited drug-likeness despite its favorable predicted CYP interaction profile.

#### *3.10.3. Ligand 3: Ellagic acid (CID 5281855)*

Ellagic acid ($C_{14}H_6O_8$; MW: 302.19 g/mol) exhibited moderate physicochemical properties, with a TPSA of 141.34 Å$^2$ and a consensus LogP of 1.00, reflecting balanced polarity. It was predicted to have high GI absorption but not to cross the BBB and not to act as a P-glycoprotein substrate. Importantly, it was not predicted to inhibit major CYP450 isoforms (e.g., CYP1A2, CYP2C19, CYP2C9, CYP2D6, CYP3A4), indicating low metabolic liabilities. Skin permeation was low (log Kp = −7.36 cm/s).

Drug-likeness profiling showed compliance with Lipinski, Ghose, and Muegge filters, while Veber and Egan filters flagged a single violation due to its high TPSA (>131 Å$^2$). The bioavailability score was 0.55. Medicinal chemistry analysis identified one PAINS alert (catechol A) and three Brenk alerts (catechol, coumarin, polycyclic aromatic hydrocarbon). Nevertheless, ellagic acid's synthetic accessibility was favorable (3.17), suggesting that it is easier to synthesize than other polyphenolic scaffolds.

Overall, luteolin and ellagic acid demonstrated better ADMET profiles, with acceptable absorption, bioavailability scores of 0.55, and manageable synthetic accessibility. However, both were flagged for PAINS alerts and potential assay interference. Ellagic acid's high TPSA may limit permeability, whereas luteolin showed moderate metabolic liabilities via CYP inhibition. In contrast, rutin exhibited poor absorption, multiple rule violations, and low predicted bioavailability, making it the least favorable candidate.

This comparative assessment of ADMET properties across the top three ligands provided an integrated perspective on efficacy, safety, and drug-likeness.

### 3.11. Comparative summary of ADMET properties

Table 7 summarizes the pharmacokinetic and drug-likeness parameters of the top three phytochemicals—luteolin (CID 5280445), rutin (CID 5280805), and ellagic acid (CID 5281855)—that exhibited the most favorable docking affinities and stability across the selected bacterial targets.

Luteolin demonstrated the strongest binding affinity, particularly with *P. aeruginosa* LasR (2UV0; −10.8 kcal/mol), and also showed moderate interaction with *E. coli* β-lactamase (1BTL; −8.3 kcal/mol), indicating dual inhibitory potential against both QS and resistance enzymes. Rutin exhibited strong binding to the AcrBZ efflux pump chain A (−9.5 kcal/mol), but its stability decreased in pump-associated complexes, suggesting steric hindrance in intact systems. Ellagic acid displayed moderate affinity toward DNA gyrase (6F86; −8.3 kcal/mol), stabilized by hydrogen bonding and aromatic π–π stacking interactions.

**Table 7. Summary of absorption, distribution, metabolism, excretion, and toxicity properties of selected ligands**

| Parameter | Luteolin (CID 5280445) | Rutin (CID 5280805) | Ellagic acid (CID 5281855) |
|---|---|---|---|
| Formula (molecular weight) | $C_{15}H_{10}O_6$ (286.24 g/mol) | $C_{27}H_{30}O_{16}$ (610.52 g/mol) | $C_{14}H_6O_8$ (302.19 g/mol) |
| TPSA (Å$^2$) | 111.13 | 269.43 | 141.34 |
| Consensus LogP | 1.73 | − 1.51 | 1.00 |
| Gastrointestinal absorption | High | Low | Moderate |
| Blood–brain barrier permeability | No | No | No |
| P-glycoprotein substrate | No | Yes | No |
| CYP inhibition | CYP1A2, 2D6, 3A4 | None | None |
| Skin permeation (log Kp) | −6.25 cm/s | −10.26 cm/s | −7.85 cm/s |
| Drug-likeness (rule violations) | None | Multiple (e.g., Lipinski, Ghose, Egan, Muegge) | Single (TPSA>131 Å$^2$) |
| Bioavailability score | 0.55 | 0.17 | 0.55 |
| PAINS/Brenk alerts | 1/1 | 1/1 | 1/2 |
| Synthetic accessibility | 3.02 (favorable) | 6.52 (poor) | 3.25 (favorable) |
| Overall assessment | Good oral absorption; moderate CYP liabilities | Poor absorption; low drug-likeness | Moderate absorption; excellent safety profile |

Abbreviations: CID: Compound ID; CYP: Cytochrome P450; TPSA: Topological polar surface area.

As presented in Table 7, ADMET profiling revealed that luteolin possessed high GI absorption and favorable drug-likeness but showed moderate CYP-related liabilities. Rutin exhibited poor absorption and multiple rule violations, while ellagic acid displayed a balanced pharmacokinetic and safety profile with low predicted toxicity. Overall, luteolin emerged as the most potent dual-target inhibitor, whereas ellagic acid offered superior safety, highlighting both compounds as promising candidates for further *in vitro* and *in vivo* validation.

Collectively, these computational analyses offer a comprehensive view of binding affinities, stability, and pharmacokinetic profiles, forming the basis for a detailed discussion of dual-action inhibitory potential.

## 4. Discussion

The present study leveraged computational approaches to evaluate 10 African medicinal plant phytochemicals for their potential as dual-action inhibitors against MDR Gram-negative bacteria. Molecular docking, hydrophobic mapping, electrostatic analysis, solvent accessibility, bond length evaluation, and *in silico* ADMET profiling collectively provided insights into ligand–protein complementarity and potential pharmacological behavior.[24,25]

Among the screened phytochemicals, luteolin (CID 5280445) consistently exhibited the highest binding affinities, particularly against LasR (−10.8 kcal/mol) and TEM-1 β-lactamase (−8.3 kcal/mol). Its strong inhibitory potential is underpinned by a synergistic network of hydrogen bonds (e.g., SER80, ASP123, LYS173), van der Waals interactions, and π–alkyl interactions, complemented by deep ligand burial within the hydrophobic pocket.[23] The donor–donor clash observed with HIS177 was minimal and did not significantly destabilize the complex.[26] The dense hydrophobic packing and extensive electrostatic complementarity of luteolin likely account for its dual activity in attenuating QS and β-lactamase function.[27,28]

Rutin (CID 5280805) demonstrated notable affinity for the AcrB efflux pump (−9.5 kcal/mol) in chain A, although the pump-associated form exhibited reduced binding due to steric hindrance.[29] Stabilization was mediated primarily by hydrogen bonds and van der Waals interactions, with π–alkyl interactions reinforcing hydrophobic complementarity. The observed reduction in binding affinity within the efflux pump context highlights the dynamic influence of protein multimerization on ligand accommodation.[25]

Ellagic acid (CID 5281855) effectively targeted DNA gyrase B (−8.3 kcal/mol), forming stable hydrogen bonds with GLU274 and LYS305, along with π–π stacking and π–anion interactions, indicating potential interference with bacterial replication.[26,30] Partial solvent exposure and moderate hydrophobic stabilization align with its intermediate binding affinity, suggesting a balance between accessibility and pocket encapsulation.[28]

Ramachandran plot analyses confirmed the structural reliability of all protein targets,[24,25] ensuring accurate docking predictions. Hydrophobic mapping and SAS analyses consistently correlated ligand burial with binding strength,[31,32] underscoring the importance of complementary non-polar interactions in complex stabilization. Bond length evaluations further reinforced the stability of top-scoring complexes, with hydrogen bonds in the 2.6–3.0 Å range mitigating the effect of minor unfavorable contacts.[33]

Both ADMET and drug-likeness predictions revealed that luteolin, despite high GI absorption and favorable drug-likeness, displayed potential mitochondrial and metabolic liabilities.[26,28] In contrast, rutin and ellagic acid generally exhibited safer pharmacokinetic and toxicity profiles,[31,33] although rutin showed moderate nephrotoxicity and immunotoxicity.[30] These findings highlight a critical trade-off between binding potency and predicted systemic safety, guiding prioritization for experimental validation.[28]

It is important to note that these predictions are computational and do not substitute for experimental toxicity assessments. The actual cytotoxicity and therapeutic safety of luteolin, rutin, and ellagic acid against human cells and MDR bacteria remain to be established through *in vitro* and *in vivo* studies.

Overall, luteolin, rutin, and ellagic acid were identified as promising computational leads with complementary inhibitory mechanisms against MDR Gram-negative bacteria.[34] The dual-action potential of these phytochemicals, targeting both virulence factors and essential bacterial enzymes, demonstrates the translational value of African medicinal plant scaffolds in rational antimicrobial design.[10] Subsequent *in vitro* and *in vivo* studies are warranted to confirm efficacy, optimize safety, and explore synergistic combinations for novel anti-MDR therapeutics.[35]

## 5. Conclusion

This study demonstrates that African medicinal plant phytochemicals possess significant dual-action potential against MDR Gram-negative bacteria. Luteolin exhibited strong binding to both LasR and TEM-1 β-lactamase, suggesting simultaneous QS disruption and enzyme inhibition. Rutin and ellagic acid showed high affinities

for the AcrB efflux pump and DNA gyrase B, respectively, indicating complementary mechanisms to impair bacterial survival and resistance. *In silico* ADMET and drug-likeness analyses further highlighted luteolin, rutin, and ellagic acid as promising leads with generally favorable pharmacokinetic profiles and manageable toxicity risks.[20] Collectively, these findings provide a computational foundation for prioritizing these phytochemicals in experimental studies aimed at developing novel anti-MDR therapeutics. Although the data suggest that these flavonoids could serve as promising antimicrobial agents, their safety, cytotoxicity, and actual antimicrobial efficacy still require experimental confirmation. Future *in vitro* and *in vivo* studies are essential before any therapeutic claims can be made.

## Acknowledgments

The authors appreciate the collaborative support of the Chemistry Collaborative Research Environment (CHEM-CORE) for providing and enabling an academic network for interdisciplinary research discussions and technical guidance during manuscript preparation.

## Funding

None.

## Conflict of interest

The authors declare that they have no competing interests.

## Author contributions

*Conceptualization:* Kanayo Samuel Okonji
*Data curation:* Prachi Dash
*Formal analysis:* All authors
*Investigation:* Prachi Dash
*Methodology:* All authors
*Supervision:* Kanayo Samuel Okonji
*Visualization:* All authors
*Writing–original draft:* Kanayo Samuel Okonji
*Writing–review & editing:* All authors

## Ethics approval and consent to participate

Not applicable.

## Consent for publication

Not applicable.

## Availability of data

All data generated or analyzed during this study are included in this manuscript.

## Further disclosure

A portion of this research was presented as a conference abstract and poster at a scientific meeting prior to submission of this manuscript: In Silico Study of Bioactive African Phytochemical Diversity for Dual-Target Drug Discovery Against MDR Gram-Negative Bacteria, International Conference cum Workshop on Global Summit on Innovative Drug Design, Discovery, and Translational Research at Puducherry, India on October 29-31 2025; Computational Discovery of Dual-Mechanism Natural Scaffolds Against MDR Gram-Negative Pathogens, 1st International Conference on Green Chemistry and Sustainable Development–ACS-Federal University Otuoke Conference 2025 at Federal University Otuoke, Bayelsa State, Nigeria on November 4–7, 2025. The current manuscript, however, represents the full, peer-reviewed version of the work, which has not been previously published or deposited in any preprint server.

## References

1. Ventola CL. The antibiotic resistance crisis: Part 1: Causes and threats. *P T*. 2015;40(4):277-283.
2. Rice LB. Federal funding for the study of antimicrobial resistance in nosocomial pathogens: No ESKAPE. *J Infect Dis*. 2008;197(8):1079-1081.
   doi: 10.1086/533452
3. World Health Organization (WHO). *Global Priority List of Antibiotic-Resistant Bacteria to Guide Research, Discovery, and Development of New Antibiotics*; 2017. Available from: https://www.who.int/publications/i/item/WHO-EMP-IAU-2017.12
4. Theuretzbacher U. Accelerating resistance, inadequate antibacterial drug pipelines and international responses. *Int J Antimicrob Agents*. 2012;39(4):295-299.
   doi: 10.1016/j.ijantimicag.2011.12.006
5. Newman DJ, Cragg GM. Natural products as sources of new drugs over the last 25 years. *J Nat Prod*. 2007;70(3):461-477.
   doi: 10.1021/np068054v
6. Thakur BK, Malaise Y, Choudhury SR, *et al*. Dietary fibre counters the oncogenic potential of colibactin-producing *Escherichia coli* in colorectal cancer. *Nat Microbiol*. 2025;10(4):855-870.
   doi: 10.1038/s41564-025-01938-4
7. Iwu MM, Duncan AR, Okunji CO. New antimicrobials of plant origin. In: Janick J, editor. *Perspectives on New Crops and New Uses*. Maryland: ASHS Press; 1999. p. 457-462.
8. Akinmoladun FO, Akinrinlola BL, Komolafe FO, Farombi EO. African medicinal plants with antimicrobial activities against antibiotic-resistant bacteria: A review. *Front*

*Pharmacol*. 2020;11:585267.

doi: 10.3389/fphar.2020.585267

9. Kitchen DB, Decornez H, Furr JR, Bajorath J. Docking and scoring in virtual screening for drug discovery: Methods and applications. *Nat Rev Drug Discov*. 2004;3(11):935-949.

doi: 10.1038/nrd1549

10. Daina A, Michielin O, Zoete V. SwissADME: A free web tool to evaluate pharmacokinetics, drug-likeness and medicinal chemistry friendliness of small molecules. *Sci Rep.* 2017;7(1):42717.

doi: 10.1038/srep42717

11. Nazzaro F, Fratianni F, Coppola R, De Feo V. Essential oils and antifungal activity. *Pharmaceuticals (Basel)*. 2017;10(4):86.

doi: 10.3390/ph10040086

12. Breland EJ, Eberly AR, Hadjifrangiskou M. An Overview of two-component signal transduction systems implicated in extra-intestinal pathogenic *E. coli* Infections. *Front Cell Infect Microbiol*. 2017;7:162.

doi: 10.3389/fcimb.2017.00162

13. Rutherford ST, Bassler BL. Bacterial quorum sensing: Its role in virulence and possibilities for its control. *Cold Spring Harb Perspect Med*. 2012;2(11):a012427.

doi: 10.1101/cshperspect.a012427

14. Li YH, Tian X. Quorum sensing and bacterial social interactions in biofilms. *Sensors (Basel)*. 2012;12(3):2519-2538.

doi: 10.3390/s120302519

15. Cushnie TP, Lamb AJ. Antimicrobial activity of flavonoids. *Int J Antimicrob Agents*. 2005;26(5):343-356.

doi: 10.1016/j.ijantimicag.2005.09.002

16. Farhadi K, Khoshbakht T, Hatami M. Inhibitory effects of coumarin derivatives on bacterial DNA gyrase: Molecular docking study. *J Mol Graph Model*. 2016;66:172-180.

17. Guo Y, Sun C, Zhu W, Liu Y. Inhibition of beta-lactamase by plant polyphenols: Potential use in combination with beta-lactam antibiotics. *BMC Microbiol*. 2014;14:282.

doi: 10.1186/s12866-014-0282-3

18. Pettersen EF, Goddard TD, Huang CC, *et al*. UCSF Chimera--a visualization system for exploratory research and analysis. *J Comput Chem*. 2004;25(13):1605-1612.

doi: 10.1002/jcc.20084

19. Dallakyan S, Olson AJ. Small-molecule library screening by docking with PyRx. *Methods Mol Biol*. 2015;1263:243-250.

doi: 10.1007/978-1-4939-2269-7_19

20. Kumar M, Rathore RS. RamPlot: A webserver to draw 2D, 3D and assorted Ramachandran (ϕ, ψ) maps. *J Appl Cryst*. 2025;58:630-636.

doi: 10.1107/s1600576725001669

21. O'Boyle NM, Banck M, James CA, Morley C, Vandermeersch T, Hutchison GR. Open Babel: An open chemical toolbox. *J Cheminform*. 2011;3:33.

doi: 10.1186/1758-2946-3-33

22. Trott O, Olson AJ. AutoDock Vina: Improving the speed and accuracy of docking with a new scoring function, efficient optimization, and multithreading. *J Comput Chem*. 2010;31(2):455-461.

doi: 10.1002/jcc.21334

23. BIOVIA, Dassault Systèmes. *Discovery Studio Visualizer*. San Diego, CA: Dassault Systèmes; 2021.

24. Geng YF, Wang Y, Zhang Y, *et al*. An innovative role for luteolin as a natural quorum sensing inhibitor in *Pseudomonas aeruginosa*. *Sci Rep.* 2021;11(1):12562.

doi: 10.1038/s41598-021-91891-2

25. Singh G, Hossain MA, Al-Fahad D, *et al*. An *in-silico* approach to target multiple proteins involved in anti-microbial resistance using natural compounds produced by wild mushrooms. *Biochem Biophys Rep.* 2024;40:101854.

doi: 10.1016/j.bbrep.2024.101854

26. Vargiu AV, Nikaido H. Multidrug binding properties of the AcrB efflux pump characterized by molecular dynamics simulations. *Proc Natl Acad Sci U S A*. 2012;109(50):20637-20642.

doi: 10.1073/pnas.1218348109

27. Jamshidi S, Rahman KM, Sutton JM. Mapping the dynamic functions and structural features of AcrB efflux pump transporter using accelerated molecular dynamics simulations. *Sci Rep.* 2018;8(1):10470.

doi: 10.1038/s41598-018-28531-6

28. García Hernández LC, Higuera-Piedrahita RI, Rivero-Perez N, *et al*. Antibacterial activity and molecular docking of lignans isolated from *Artemisia cina* against multidrug-resistant bacteria. *Pharmaceuticals (Basel)*. 2025;18(6):781.

doi: 10.3390/ph18060781

29. Alhussaini HAM, Alhussaini M, Alhussaini M. Ellagic acid's 3D binding modes in DNA gyrase's ATP active site. *J Mol Graph Model*. 2024;112:108108.

30. Jamshidi S, Sutton JM, Rahman KM. Mapping the dynamic functions and structural features of AcrB efflux pump transporter using accelerated molecular dynamics simulations. *Sci Rep.* 2018;8(1):10470.

doi: 10.1038/s41598-018-28531-6

31. Weinder-Wells MA, Altom J, Fernandez J, *et al*. DNA gyrase

inhibitory activity of ellagic acid derivatives. *Bioorg Med Chem Lett*. 1998;8(1):97-100.

doi: 10.1016/s0960-894x(97)10197-4

32. Wilson DN. Ribosome-targeting antibiotics and mechanisms of bacterial resistance. *Nat Rev Microbiol*. 2014;12(1):35-48.

doi: 10.1038/nrmicro3155

33. Guo Y, Zhang Y, Wang Y, *et al*. PknB and STP as potential targets of luteolin in combating *Mycobacterium tuberculosis*: Computational investigation. *Comput Biol Chem*. 2025;101:107807.

doi: 10.1016/j.compbiolchem.2025.107807

34. Bekeir H, Hamad A, Eleiwa NZ, Amin RA. Molecular docking analysis of the antibacterial effect of pomegranate (*Punica granatum*) fruit molasses bioactive compounds. *Benha Vet Med J*. 2024;46(2):90-95.

doi: 10.21608/bvmj.2024.284813.1816

35. Banerjee P, Eckert AO, Schrey AK, Preissner R. ProTox-II: A webserver for the prediction of toxicity of chemicals. *Nucleic Acids Res*. 2018;46(W1):W257-W263.

doi: 10.1093/nar/gky318